Role of the dopant aluminum for the growth of sputtered ZnO:Al investigated by means of a seed layer concept

Nicolas Sommer,[1, a)] Mishael Stanley,[1] Florian Köhler,[1] Jan Mock,[1] and Jürgen Hüpkes[1]
IEK5 - Photovoltaik, Forschungszentrum Jülich GmbH, 52425 Jülich

(Dated: April 27, 2015)

This work elucidates the effect of the dopant aluminum on the growth of magnetron-sputtered aluminum-doped zinc oxide (ZnO:Al) films by means of a seed layer concept. Thin ($< 100\,\mathrm{nm}$), highly doped seed layers and subsequently grown thick ($\sim 800\,\mathrm{nm}$), lowly doped bulk films were deposited using a $ZnO:Al_2O_3$ target with 2 wt% and 1 wt% Al_2O_3, respectively. We investigated the effect of bulk and seed layer deposition temperature as well as seed layer thickness on electrical, optical, and structural properties of ZnO:Al films. A reduction of deposition temperature by 100 °C was achieved without deteriorating conductivity, transparency, and etching morphology which renders these low-temperature films applicable as light-scattering front contact for thin-film silicon solar cells. Lowly doped bulk layers on highly doped seed layers showed smaller grains and lower surface roughness than their counterpart without seed layer. We attributed this observation to the beneficial role of the dopant aluminum that induces an enhanced surface diffusion length via a surfactant effect. The enhanced surface diffusion length promotes 2D-growth of the highly doped seed layer which is then adopted by the subsequently grown and lowly doped bulk layer. Furthermore, we explained the seed layer induced increase of tensile stress on the basis of the grain boundary relaxation model. The model relates the grain size reduction to the tensile stress increase within the ZnO:Al films. Finally, temperature-dependent conductivity measurements, optical fits, and etching characteristics revealed that seed layers reduced grain boundary scattering. Thus, seed layers induced optimized grain boundary morphology with the result of a higher charge carrier mobility and more suitable etching characteristics. It is particularly compelling that we observed smaller grains to correlate with an enhanced charge carrier mobility. A seed layer thickness of 5 nm was sufficient to induce the beneficial effects.

I. INTRODUCTION

Transparent conductive oxides (TCO) combine electrical conductivity and transparency in the visible range. These unique properties result in a wide variety of applications such as low-emissivity, electrochromic, and smart windows[1,2], as well as optoelectronic devices such as flat panel displays[3], organic light emitting diodes, and solar cells[4–6].

A prominent TCO representative is aluminum-doped ZnO (ZnO:Al). It consists of abundant and non-toxic elements. ZnO:Al is applied in thin-film silicon[7,8] and chalcopyrite based solar cells[9,10] as transparent front contact. The application as front contact requires high conductivity and transparency. Furthermore, the contact layer needs to be textured particularly with regard to the application in thin-film silicon solar cells[8,11,12]. The textured surface induces an elongated light path within the thin absorber layer that facilitates absorption. As a result, short-circuit current density and thus the solar cell's conversion efficiency increase. Besides self-textured TCOs such as SnO_2:F or ZnO:B[13], textured contact layers are produced by a post-deposition etching step of sputter-deposited ZnO:Al[7,14,15].

To ensure an etching morphology with appropriate light scattering properties, a careful adjustment of ZnO:Al deposition parameters such as pressure, temperature[16], film thickness[17], and target doping concentration (TDC)[8] is needed. However, conflicting requirements in terms of ZnO:Al deposition conditions prevail since conductivity, transparency, and surface texture need to be optimized simultaneously. This contribution addresses the tradeoff between deposition temperature and TDC. The most suitable TDCs in terms of transparency are 0.5 - 1 wt% of Al_2O_3[8]. Yet these lower TDCs as compared to the standard TDC of 2 wt% need elevated deposition temperatures in order to obtain a suitable etching morphology and a high charge carrier mobility that compensates the lower charge carrier concentration.

We have chosen a seed layer concept in order to reduce the deposition temperature of ZnO:Al layers sputtered with low TDCs because various seed layer approaches have been shown to ameliorate ZnO growth[18–21].

Köhl et al. used ion beamed assisted sputtering to improve the c-axis orientation of ZnO deposited at room temperature[18,19]. The Xe^+ ion bombardment induced highly oriented grains already in the nucleation stage of the growth process via an atomic peening mechanism[22,23]. A competitive growth mode of the subsequently deposited layer was suppressed without further ion bombardment because the film adopted the preferential orientation of the seed layer.

Dewald et al. aimed at producing suitable ZnO:Al layers for solar cell applications with high deposition rate processes using direct current (dc) sputtering[20]. However, a simple dc-process did not yield the desired results especially with regard to the etch morphology. There-

[a)] n.sommer@fz-juelich.de; http://www.fz-juelich.de/iek/iek-5/EN/Home/home_node.html

fore, they applied a low rate, radio frequency (rf) sputtering process to deposit a thin seed layer knowing that the rf-process leads to films with suitable etching morphology. Indeed, dc-sputtered films deposited on top of rf-grown layers showed appropriate etching characteristics and improved electrical properties.

Claeyssens et al. deposited ZnO films by pulsed laser deposition (PLD) using a high-temperature seed layer[21]. Increasing the deposition temperature to a certain limit improved the grain orientation and crystal structure. Therefore, they applied an optimized high-temperature seed layer whose ameliorated film structure determined the further low-temperature ZnO growth.

The seed layer used in this work consisted of a thin layer sputtered from a target with TDC of 2 wt%. Subsequently, a lowly doped bulk layer was deposited using a TDC of 1 wt%. This approach aims at combining the low deposition temperatures of highly doped ZnO:Al (TDC=2 wt%) with the high transparency of lowly doped ZnO:Al (TDC=1 wt%) while maintaining high conductivity and appropriate etching morphology.

The objectives of this contribution are fourfold:
(1) We will prove that the above proposed seed layer approach is in fact applicable to reduce ZnO:Al deposition temperature without deteriorating electro-optical and etching properties.
(2) We will elucidate the effect of aluminum for ZnO:Al growth.
(3) Tensile stress within the ZnO:Al films will be explained to result from a reduction of grain size.
(4) We will show that the charge carrier mobility in films with and without seed layer is limited by different scattering mechanisms. Based hereupon, we provide evidence for the counterintuitive hypothesis that smaller lateral grain sizes in our ZnO:Al films lead to a higher charge carrier mobility.[24]

II. EXPERIMENTAL DETAILS

ZnO:Al seed layers were deposited in a magnetron sputtering system (*Lesker Inc., USA*) in static radio frequency mode from a ceramic target with a target doping concentration (TDC) of 2 wt% Al_2O_3. ZnO:Al bulk layers were dynamically deposited in a vertical inline sputter deposition system (*VISS 300, VAAT, Germany*) from a ceramic target with a TDC of 1 wt% Al_2O_3. Bulk layer growth on various seed layers was conducted in a single deposition process to assure good comparability. The systems' base pressure was about 2×10^{-7} mbar. The temperatures presented in this paper are heater temperatures. For both deposition systems, substrates temperatures were roughly two third of the heater temperatures. The deposition pressure was 0.3 Pa in the case of seed layers and 0.1 Pa for bulk layers. All layers were prepared on cleaned glass substrates (*Corning Eagle XG*). Etching of ZnO:Al was performed in 0.5 wt% hydrochloric acid (HCl).

We measured the layer thickness with a surface profiler (*Dektak 3030, Veeco, USA*). Electrical properties were determined by Hall effect measurements in van der Pauw geometry. Room temperature measurements were performed in a commercial setup *RH2030 (PhysTech, Germany)*. Temperature-dependent Hall effect measurements relied on a home-made experiment using liquid nitrogen. A magnetic field of 2.1 T was used. Further details about this measurement setup can be found elsewhere[25].

The surface morphology was investigated by scanning electron microscopy (SEM) in a *LEO 1550 VP GEMINI (Zeiss, Germany)* and by atomic force microscopy (AFM) in a *Nanostation 300 (SIS, Germany)* using contact mode. Tips with radii smaller than 10 nm were used to resolve smallest features. At least three images were recorded for every sample. Post-processing and the computation of the root mean square (rms) roughness and the height-height correlation length (HHCL) of the surfaces were conducted with the program *Gwyddion*. Post-processing steps of the raw data comprised (1) leveling by mean plane subtraction, (2) correcting lines by matching height median, and (3) the removal of a polynomial background with a maximum polynomial degree of two. The HHCL was deduced from a Gaussian fit of the height-height correlation function. SEM images of etched ZnO:Al layers were recorded using a sample tilt of 45° to get a better 3D impression of the sample surface.

Optical transmittance T and reflectance R of flat films have been measured with a dual beam spectrometer *Lambda 950* (*Perkin Elmer, USA*). The absorptance A has been calculated using the relation $A = 1 - T - R$.

For structural investigations, x-ray diffraction (XRD) measurements in Bragg-Brentano (BB) and rocking curve (RC) geometry were performed using a diffractometer *D8 Advance (Bruker)*.

Microcrystalline silicon (μc-Si:H) solar cells were prepared in a plasma enhanced chemical vapour deposition (PECVD) process to investigate the performance of ZnO:Al with seed layer approach in solar cells. Details of this process can be found elsewhere[26,27]. Sputtered ZnO:Al and silver were used as back contact. *I-V* measurements were performed in a class A sun simulator under AM1.5.

Modeling of transmittance and reflectance spectra has been performed with the program SCOUT[28] using a harmonic oscillator, a modified Drude model, and an O'Leary-Johnson-Lim (OJL) model. The modified Drude model comprised a frequency-dependent damping factor

$$\Gamma_{\mathrm{Dr}}(\omega) = \Gamma_{\mathrm{L}} - \frac{\Gamma_{\mathrm{L}} - \Gamma_{\mathrm{H}}}{\pi} \left[\arctan\left(\frac{\omega - \Omega_{\Gamma\mathrm{Dr}}}{\Gamma_{\Gamma\mathrm{Dr}}}\right) + \frac{\pi}{2}\right], \tag{1}$$

which is described by the low-frequency (Γ_{L}, $\omega = 0$) and high-frequency (Γ_{H}, $\omega = \infty$) damping factors, the changeover frequency $\Omega_{\Gamma\mathrm{Dr}}$ and the function width $\Gamma_{\Gamma\mathrm{Dr}}$. More details about this model approach can be found in Mergel et al.[29] and Qiao et al.[30].

We can derive the resistivity

$$\rho_{\mathrm{opt}} = \left[\epsilon_0\, \Omega_{\mathrm{Dr}}^2 \Gamma_{\mathrm{Dr}}(\Omega_{\mathrm{Dr}})\right]^{-1} \quad (2)$$

by the modeling of optical spectra. Here, $\Gamma_{\mathrm{Dr}}(\Omega_{\mathrm{Dr}})$ and Ω_{Dr} denote the plasma frequency and the damping frequency, respectively. ϵ_0 is the vacuum permittivity. Instead of ρ_{opt}, most authors compute the mobility μ_{opt}[29–40]. The determination of μ_{opt} by modeling of optical spectra requires the effective mass m^*, whereas the resistivity ρ_{opt} can be evaluated without knowing m^*. As the effective mass is prone to considerable uncertainties[30,35,36,40], we will focus on the resistivity ρ_{opt}. Error bars were obtained by fitting the same spectrum several times with different starting conditions. Note furthermore that we evaluated the damping frequency Γ_{Dr} at the plasma frequency Ω_{Dr} to obtain ρ_{opt}, whereas several authors determined μ_{opt} or ρ_{opt} by using the low-frequency damping constant Γ_{L}[37–41]. Our evaluation is in line with the original publication of Mergel et al.[29] and we will see that the obtained resistivity values are reasonable within the general understanding of conductivity in the investigated material.

III. RESULTS

Three different parameter series have been performed to evaluate the seed layer impact on the subsequently grown bulk layer. First, the process temperature during bulk deposition T_{bulk} was varied keeping the seed layer constant. Second, seed layer deposition temperature T_{seed} and, third, seed layer thickness d_{seed} were changed using the same bulk deposition parameters.

A. Bulk layer: temperature variation

We evaluated the influence of T_{bulk} on electro-optical and etching properties of sputtered ZnO:Al grown on seed layers. The deposition conditions for the seed layer sputtered from a target with TDC = 2 wt% remained constant for the following evaluation. T_{seed} and d_{seed} were 250 °C and 40 nm, respectively. T_{bulk} was varied from 100 °C to 430 °C. The bulk layer thickness was approximately 800 nm.

temperature T_{bulk} [°C]	mobility μ [cm²/Vs]		carrier concentration n x 10^{20}[cm^{-3}]	
	seed	no seed	seed	no seed
100	27.1	27.3	2.6	2.8
200	32.5	30.3	3.2	3.5
300	36.0	17.4	4.5	3.9
430	46.4	46.4	5.3	5.6

Table I. Charge carrier mobility and concentration for four different bulk deposition temperatures T_{bulk} with and without seed layer. Seed layer deposition parameters were: $d_{\mathrm{seed}} = 40$ nm, $T_{\mathrm{seed}} = 350$ °C.

The electrical properties of bulk layers deposited at various temperatures with and without seed layer are summarized in Table I. For $T_{\mathrm{bulk}} = 100$ °C, $T_{\mathrm{bulk}} = 200$ °C, and $T_{\mathrm{bulk}} = 430$ °C, the seed layer influenced charge carrier mobility and concentration only very slightly. In contrast, for $T_{\mathrm{bulk}} = 300$ °C, we noticed a significantly higher charge carrier mobility and concentration for samples with seed layer in comparison to samples without seed layer. The severe mobility gap is predominantly caused by the mobility drop of the sample without seed layer. The seed layer prevented this mobility drop. Note that we also reported on the aforementioned mobility gap in another publications[42].

Figure 1(a) shows the transmittance and absorptance of smooth films deposited at various T_{bulk}. In the wavelength range close to the band gap around 400 nm, the absorptance shifted to longer wavelengths due to a decrease of carrier concentration (confirmed by Hall measurements, see Table I) resulting in a Burstein-Moss shift. A slight change in the slope of the curves however hints to additional sub band gap absorptance probably related to additional defects caused by the lower T_{bulk}[43]. In general, the absorptance of samples employing a seed layer in combination with low deposition temperatures was higher in the wavelength range between 350 nm and 600 nm in comparison to the high-temperature reference ($T_{\mathrm{bulk}} = 430$ °C) without seed layer. Yet, the seed layer induced lower absorptance compared to films deposited at the same T_{bulk} but without seed layer (see Fig. 1(b)). Indeed, the absorptance reduction was to a large fraction determined by the lower sub band gap absorptance as can be deduced from the steeper slope of the seed layer curves.

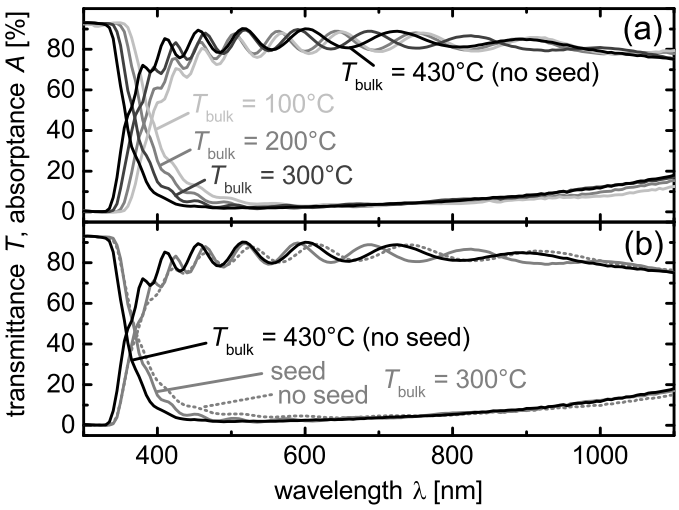

Figure 1. Transmittance and absorptance of ZnO:Al layers: (a) Bulk layers deposited at three different T_{bulk} in combination with a seed layer ($d = 40$ nm, $T_{\mathrm{seed}} = 350$ °C) were measured. (b) Bulk layers using $T_{\mathrm{bulk}} = 300$ °C were deposited with and without seed layer. For comparison, both graphs show a standard high-temperature process ($T_{\mathrm{bulk}} = 430$ °C) without seed layer.

Figure 2 shows the morphology after etching for 40 s in dilute HCl. The films without seed layer showed a surface with small, grainy structures except for $T_{\mathrm{bulk}} = 430\,^{\circ}\mathrm{C}$. We determined the grainy surface texture to be of Type A after the modified Thornton model of Kluth et al.[16]. The application of seed layers induced a crater-like morphology already for T_{bulk} as low as 100 °C. The crater-like surface texture, also called Type B following Kluth et al., was fully developed for T_{bulk} exceeding 200 °C.

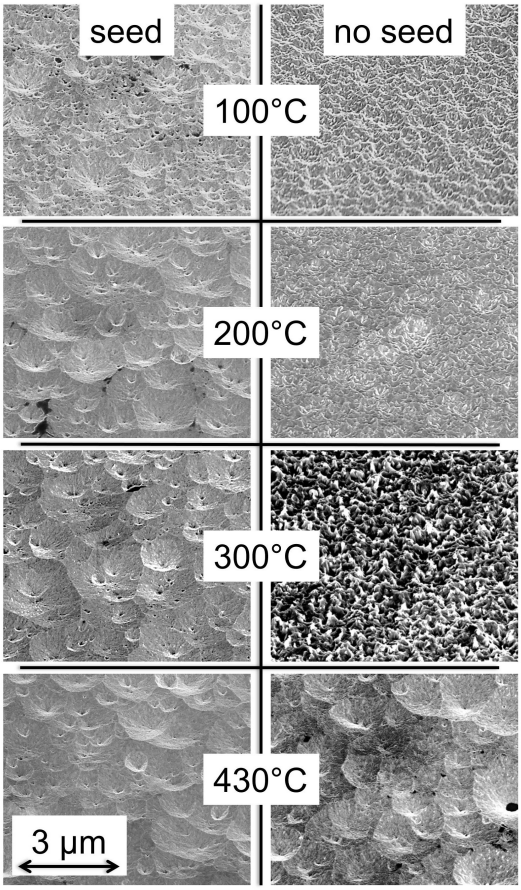

Figure 2. SEM images of etched ZnO:Al layers. T_{bulk} was varied from 100 °C to 430 °C (top to bottom). References without seed layer (right column) and samples with seed layers ($d = 40\,\mathrm{nm}$, $T_{\mathrm{seed}} = 350\,^{\circ}\mathrm{C}$, left column) were co-deposited.

B. Seed layer: temperature variation

We selected $T_{\mathrm{bulk}} = 300\,^{\circ}\mathrm{C}$ in order to investigate the influence of T_{seed} on the subsequently deposited bulk layer. Bulk layers grown at $T_{\mathrm{bulk}} = 300\,^{\circ}\mathrm{C}$ in conjunction with seed layers offered reasonable optical and etching properties. Also, the seed layers showed a prominent influence on the electrical properties for the selected T_{bulk}. The seed layer thickness was 40 nm. T_{seed} was varied from 250 °C to 450 °C in 50 °C steps.

The influence of T_{seed} on electrical properties at room temperature is summarized in Fig. 3. Charge carrier mobility (a) and concentration (b), and resistivity (c) were determined by Hall effect measurements. The resistivity was additionally determined by optical fits in order to differentiate between intra-grain scattering ρ_{g} and inter-grain, i.e. grain boundary scattering ρ_{gb}. Following Matthiessen's rule, both scattering components add up to the total resistivity of the film $\rho_{\mathrm{tt}} = \rho_{\mathrm{g}} + \rho_{\mathrm{gb}}$. Hall effect measurements determine the film's total resistivity because the current is forced to flow through grains and grain boundaries. In contrast, optical measurements induce an electric field that causes the charge carriers to oscillate within a few nanometers. As the average electron path length is smaller than the grain size, the charge carriers are only scattered within the grain and hardly at grain boundaries[31,33,40]. Thus, the determination of electrical properties using both techniques, Hall effect measurements and optical fits, enables us to identify the relative fraction of intra-grain and inter-grain scattering.

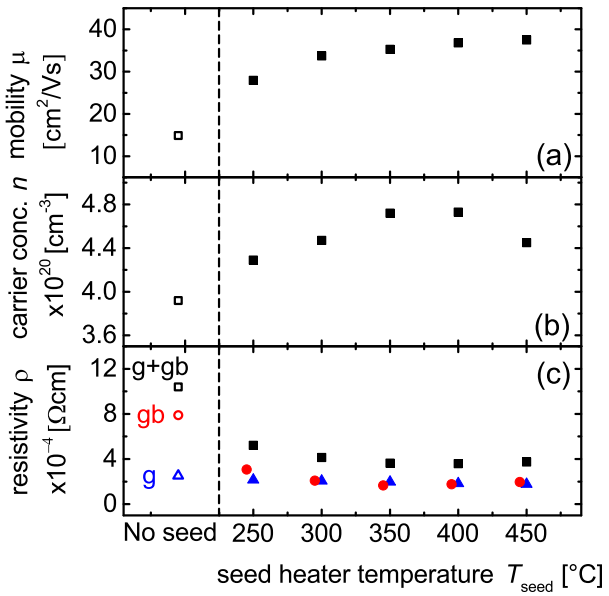

Figure 3. Charge carrier mobility (a) and concentration (b), and resistivity (c) for a sample without seed layer (open symbols) and samples with seed layer (closed symbols). Black squares and blue triangles are data points derived from Hall effect measurements and optical fits, respectively. In figure (c), we used Matthiessen's rule $\rho_{\mathrm{tt}} = \rho_{\mathrm{g}} + \rho_{\mathrm{gb}}$ to split up the resistivity derived from Hall effect measurements (g+gb) into the part belonging to the intra-grain scattering (g) derived from optical fits and a part belonging to grain boundary scattering (gb). Note that the gb-data is slightly shifted to assure better clarity.

Application of seed layers induced a mobility increase of more than a factor 2 (Fig. 3(a)), e.g. the sample without seed layer showed a mobility of $15\,\mathrm{cm}^2/\mathrm{Vs}$ whereas a seed layer grown at 350 °C resulted in a mobility of $35\,\mathrm{cm}^2/\mathrm{Vs}$. The carrier concentration (Fig. 3(b)) was

higher for seed layer samples. It increased with temperature up to 400 °C and then dropped slightly. The Hall resistivity (Fig. 3(c), black squares) was dominated by the increase of Hall mobility. It decreased with the use of seed layers by a factor of 3. The optically determined resistivity (Fig. 3(c), blue triangles) however decreased only by about 20%. The slightly changed intra-grain resistivity implies seed layers to mainly influence grain boundary scattering. Indeed, seed layers induced a reduction of grain boundary scattering in the subsequently deposited bulk layers. The share of resistivity attributed to grain boundary scattering (red circles in Fig. 3(c)) decreased by a factor of 4 when a seed layer grown at 350 °C was applied.

Figure 4 shows the temperature-dependent conductivity of samples without (circles) and with seed layer grown at 350 °C (squares). The obtained data was fitted with a conductivity model that takes into account three different scattering mechanisms: ionized impurity, electron-phonon, and grain boundary scattering. Ionized impurity scattering was described by the theory of Brooks[44] and Herring, and Dingle[45]. The analytical expression for the screening function was taken from Pisarkiewicz et al.[46]. We assumed the films to be uncompensated. Values for the effective mass were taken from Ruske et al.[40]. Electron-phonon scattering is implemented by the Bloch-Grüneisen law[47–49]. Grain boundary scattering is described by quantum mechanical tunneling of electrons through potential barriers at grain boundaries. For this purpose, we adapted expressions from Stratton[50,51]. Note that the complete conductivity model comprises of merely three fit parameters. The conductivity model and in particular the electron tunneling at grain boundaries will be described in more detail elsewhere[52].

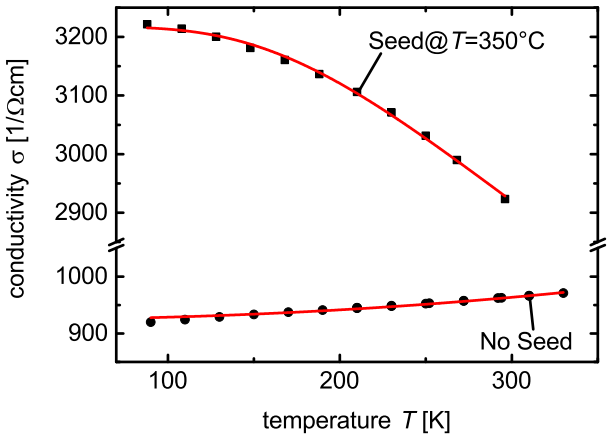

Figure 4. Temperature-dependent conductivity measurements: A sample without seed layer (circles) and a sample with seed layer deposited at 350 °C (squares) were investigated. Red lines are fits using a conductivity model comprising ionized impurity, electron-phonon, and grain boundary scattering. Grain boundary scattering was described by tunneling through potential barriers at grain boundaries.

The seed layer sample showed a decreasing conductivity with raising temperature. This temperature dependence is characteristic for electron-phonon scattering. Note however that the overall conductivity level was determined by ionized impurity and grain boundary scattering. In contrast, the sample without seed layer could be fitted using the tunneling model at grain boundaries only. Thus, the enhanced conductivity of the seed layer sample in comparison to the sample without seed layer was due to a reduction of grain boundary scattering. In conclusion, the temperature-dependent conductivity measurements underlined the hypothesis that the application of seed layers significantly improved the charge carrier transport across grain boundaries.

Figure 5 shows transmittance and absorptance of samples without seed layer and with seed layers deposited at $T_{\mathrm{seed}} = 250\,^{\circ}\mathrm{C}$ and $T_{\mathrm{seed}} = 450\,^{\circ}\mathrm{C}$. As already presented in the previous section, the seed layer reduced the absorptance in the wavelength range between 350 nm and 600 nm in comparison to the sample without seed layer. However, the absorptance was not as low as for the high-temperature reference. A higher seed temperature induced a slight absorptance decrease. But this effect was not as pronounced as the effect that was observed when comparing samples with and without seed layer. In the long wavelength range above 800 nm, the absorptance was governed by free carrier absorption and therefore correlated with the carrier concentration.

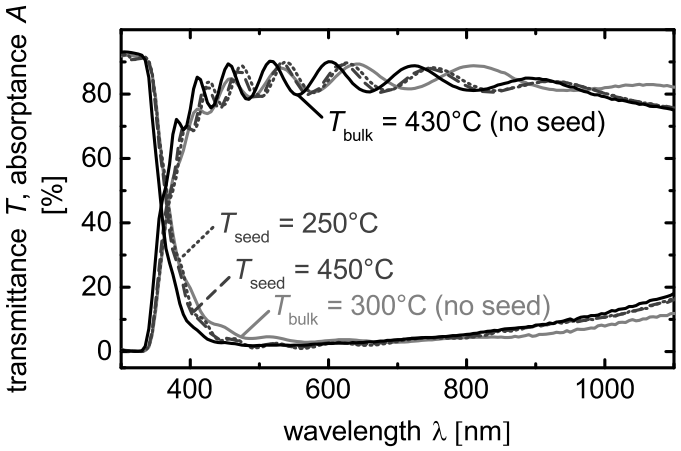

Figure 5. Transmittance and absorptance of ZnO:Al layers. A sample without seed layer (grey solid line) and two samples with seed layers (dotted and dashed lines) deposited at $T_{\mathrm{seed}} = 250\,^{\circ}\mathrm{C}$ and $T_{\mathrm{seed}} = 450\,^{\circ}\mathrm{C}$ are shown. For comparison, a standard high-temperature process ($T_{\mathrm{bulk}} = 430\,^{\circ}\mathrm{C}$) without any seed layer is plotted as well (black solid line).

Figure 6 shows SEM images of etched ZnO:Al films with and without seed layers. Without seed layer, the surface morphology was of Type A[16]. Applying a seed layer with $T_{\mathrm{seed}} = 250\,^{\circ}\mathrm{C}$, a clear change of surface texture was found compared to samples without seed layer. The texture shifted to a crater-like morphology although craters are rather small. However, increasing T_{seed} to 350 °C led to a crater-like surface texture of Type B. A

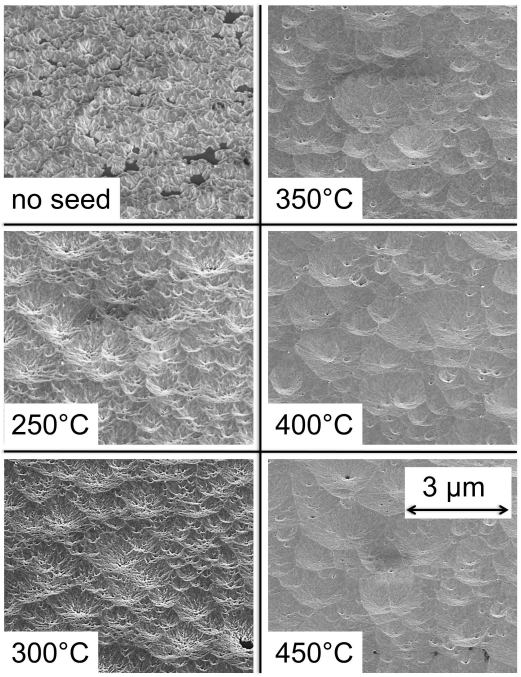

Figure 6. SEM images of etched ZnO:Al layers. T_{seed} was varied from 250 °C to 450 °C. T_{bulk} was 300 °C.

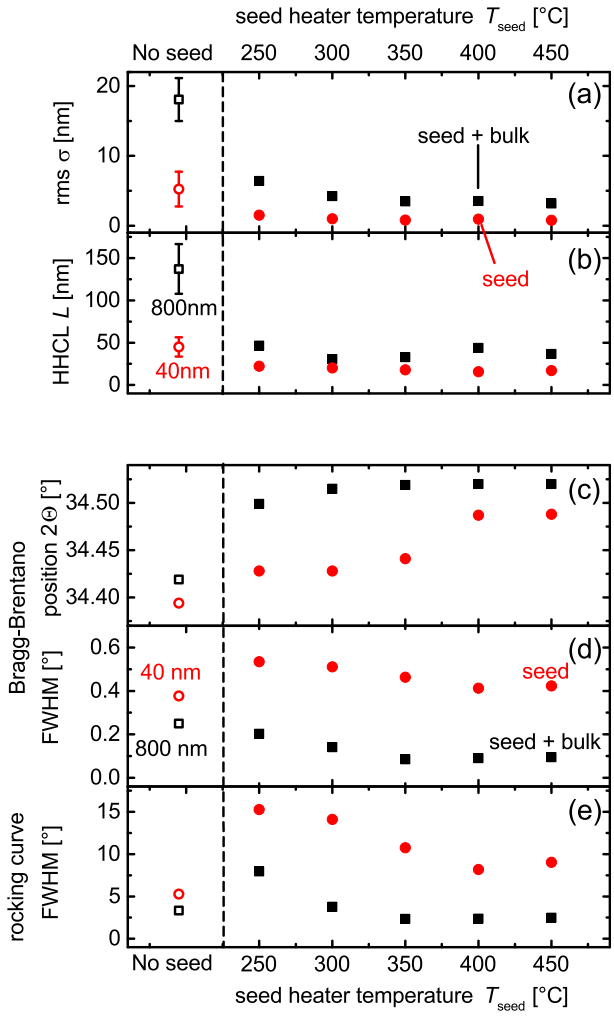

Figure 7. Samples with (closed symbols) and without seed layer (open symbols) were investigated by AFM (a), (b) and XRD (c)-(e) measurements. AFM investigations comprised of the measurement of rms roughness (a) and height-height correlation length (HHCL) (b). XRD investigations were performed in Bragg-Brentano and rocking curve geometry. Bragg-Brentano: (002) peak position (c) and FWHM (d). Rocking curve of (002) peak: FWHM (e). The 40 nm thin seed layers (closed, red circles) and the 800 nm thick combination of seed and bulk layers (closed, black squares) are shown. Bulk layer deposition conditions were used to deposit a 40 nm thin layer (open, red circles) and a 800 nm thick film (open, black squares).

further increase of T_{seed} did not alter the surface texture.

The surface morphology of flat, unetched ZnO:Al layers was measured with atomic force microscopy (AFM). Figure 7 shows the rms roughness (a) and height-height correlation length (HHCL)(b) of seed and seed+bulk layers. Red, open symbols denote 40 nm thin films that were grown using bulk layer deposition conditions. Generally, all samples exhibited a lower rms roughness and HHCL than the reference sample without seed layer. Both quantities merely showed a small decrease with increasing seed temperature. Nevertheless, the overall effect of the seed layer was pronounced. The rms roughness of the bulk reference sample without seed layer was 18.1 nm whereas the rms roughness of the seed+bulk sample with seed layer deposited at 300 °C was determined to be 4.2 nm only.

X-ray diffraction (XRD) measurements have been performed to evaluate the influence of seed layers on crystallographic properties of ZnO:Al films. Figure 7 shows the position (c) and the full width at half maximum (FWHM) (d) of the (002) peak in Bragg-Brentano (BB) geometry. The FWHM of the (002) peak determined in rocking curve (RC) geometry is depicted in Fig. 7(e). We observed for seed (red circles) and seed+bulk (black squares) layers that an increase of T_{seed} induced an increase of (002) peak position and a FWHM decrease in BB and RC geometry.

The comparison of films with and without seed layer revealed that the (002) peak position of the bulk layer without seed layer (black, open square) was smaller by approximately 0.08° in comparison to the $T_{\mathrm{seed}} = 250$ °C seed+bulk layer. Furthermore, seed layers showed for all temperatures higher BB-FWHMs compared to the thin bulk sample, whereas the BB-FWHM of seed+bulk films was slightly smaller than for the sample without seed layer. All seed layers exhibited higher RC-FWHMs than the thin bulk layer film. In contrast, RC-FWHMs of seed+bulk layers were similar or smaller than their counterpart without seed layer for T_{seed} exceeding 250 °C. Note however that the RC-FWHM of the $T_{\mathrm{seed}} = 250$ °C

seed+bulk film was more than twice as high as for the bulk film without seed layer.

C. Seed layer: thickness variation

The seed layer thickness d_{seed} was varied from 5 to 100 nm. T_{seed} and T_{bulk} were fixed at 350 °C and 300 °C, respectively.

A seed layer thickness of 5 nm was sufficient to induce the beneficial effects with regard to electrical, optical, and etching properties. A further increase of d_{seed} up to 100 nm did not alter the films' properties significantly. Exemplary, the charge carrier mobility is shown as a function of d_{seed} (Fig. 8). A strong mobility increase was observed when applying a seed layer of only 5 nm. Charge carrier concentrations of all samples were in the range of $4.7 \times 10^{20}\,\mathrm{cm}^{-3}$ to $4.9 \times 10^{20}\,\mathrm{cm}^{-3}$ and did not show any trend related to d_{seed}.

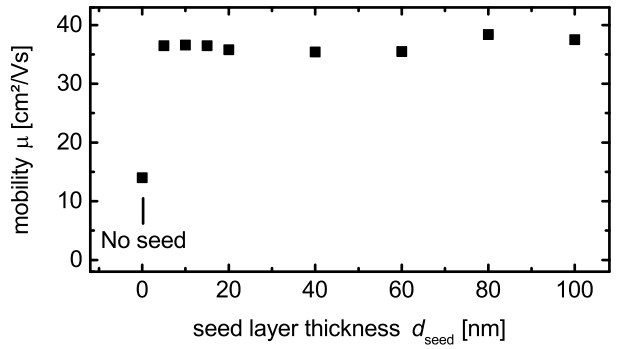

Figure 8. Charge carrier mobility μ for a sample without seed layer and films with various seed layer thicknesses d_{seed}. d_{seed} was varied from 5 nm to 100 nm. T_{seed} and T_{bulk} were 350 °C and 300 °C, respectively.

Microcrystalline silicon (μc-Si:H) solar cells were deposited on etched ZnO:Al to demonstrate the seed layer concept's applicability as light-scattering front contact. The results of seed+bulk layers and a high-temperature reference ($d_{\mathrm{seed}} = 0$ nm) are summarized in Table II. Solar cells with comparable or even slightly higher conversion efficiencies η than the high-temperature reference could be achieved on ZnO:Al with seed layer approach. Note that ZnO:Al deposition temperatures of the seed layer approach were approximately 100 °C lower than of the high-temperature reference. The open circuit voltage V_{oc} of μc-Si:H solar cells on seed+bulk layers was significantly higher compared to the reference. The fill factor FF was similar for all samples, but there was a small trend to higher fill factors for seed layers of 10 to 15 nm thickness. However, the short-circuit current density I_{sc} of seed+bulk layer samples was lower in comparison to the high-temperature reference. Moreover, the seed+bulk layer sample $d_{\mathrm{seed}} = 5$ nm exhibited lower I_{sc} than the seed+bulk layer samples with d_{seed} of 10 and 15 nm.

d_{seed} [nm]	η [%]	FF [%]	V_{oc} [mV]	I_{sc} [mA]
0	8.4	66.9	507	24.9
5	8.1	66.0	536	22.8
10	8.5	68.8	526	23.5
15	8.6	68.6	531	23.5

Table II. Solar cell parameters efficiency η, fill factor FF, open-circuit voltage V_{oc}, and short-circuit current density I_{sc} of μc-Si:H solar cells. The solar cells were deposited on etched ZnO:Al with d_{seed} of 5 to 15 nm. T_{seed} and T_{bulk} were 350 °C and 300 °C, respectively. The reference without seed layer (0 nm) was an etched, high-temperature ZnO:Al bulk film deposited at 430 °C using a TDC of 1 wt%.

IV. DISCUSSION

In the following, the beneficial effect of aluminum for the growth of aluminum-doped ZnO will be discussed in terms of the surfactant concept. Furthermore, the seed layer induced changes regarding intrinsic stress will be interpreted using the grain boundary relaxation model. Finally, an explanation for the improved electrical properties, that go along with the application of seed layers, will be presented and generalized.

A. Aluminum as surfactant

Figure 7(a) shows a reduction of rms roughness with the application of seed layers. The roughness reduction is interpreted as a transition from 3D- to 2D-growth. The transition is attributed to the beneficial role of the dopant aluminum. Other authors have also reported on the positive role of aluminum during growth of sputtered ZnO:Al[53–55]. Aluminum-doped ZnO films showed an improved (002) texture, an increased crystalline quality, and reduced intrinsic stress[53,54]. Furthermore, the rms roughness was lower for doped layers, similar to our results[55]. Boron-doped ZnO grown by low pressure chemical vapor deposition (LPCVD) also showed lower rms roughness compared to undoped films[56]. In the case of sputtered ZnO:Al, the authors speculate aluminum to act as surface-active species (surfactant)[57–59]. Surfactants are commonly applied during growth of III-V semiconductors to suppress 3D-growth. Surfactants mainly alter the surface diffusion length of the impinging atoms. Depending on the surfactant used, they can either increase or decrease the surface diffusion length[59].

In our case, we suspect aluminum to enhance the surface diffusion length. Lower deposition pressures or higher deposition temperatures increase the surface diffusion length: the former because of additional energy input into the film by means of higher ion bombardment during growth[16,53,60], the latter due to an enhancement of the thermal energy of adatoms[8,16]. Furthermore, lower deposition pressures or higher deposition temperatures induce a shift of etching morphology from Type A to Type B (see Kluth et al.[16]). Thus, lower deposition

pressures or higher deposition temperatures lead to an enhanced surface diffusion length resulting in a change of surface morphology from Type A to Type B. As seed layers with higher aluminum concentration induced exactly this change of surface morphology from Type A to Type B, we conclude that the surfactant aluminum enhances the surface diffusion length.

Note the interesting fact that higher deposition temperatures do not only enhance the surface diffusion length because of the already mentioned increase of the adatoms' thermal energy but also because of aluminum accumulation. Higher deposition temperatures induce augmented zinc evaporation from the surface. Aluminum however is not influenced as its evaporation temperature is higher than the zinc evaporation temperature. Consequently, the aluminum concentration at the surface increases for increasing deposition temperatures. Warzecha, for example, raised the concentration of the dopant gallium in ZnO:Ga films by a factor of two by increasing the deposition temperature from 25 °C to 500 °C[61]. Therefore, high deposition temperatures induce an enhancement of surface diffusion length due to two effects, namely the increased thermal energy of adatoms and the higher concentration of the surfactant aluminum.

In conclusion, the dopant aluminum acts as a surfactant that increases the surface diffusion length. As a result, 3D-growth of the highly aluminum-doped seed layer is prevented and further growth of bulk layers is ameliorated.

B. Stress formation and grain boundary relaxation model

Figure 7(c) shows the (002) peak position to increase with the application of seed layers. Under the assumption of the biaxial-strain model, we attribute the peak shift to higher angles to rising tensile stress in the xy-plane[62]. Tensile stress might be explained by the grain boundary relaxation model (GBRM)[23,63]. Interatomic attractive forces between adjacent grains impose tensile stress. One can relate the ionic radius r_0, the Young modulus E, the Poisson ratio ν and the grain size L by the expression

$$\sigma \approx \frac{\mathrm{E}}{1-\nu}\,\frac{r_0}{L} \tag{3}$$

to the tensile stress σ. Note the inverse relationship between grain size and tensile stress. In the following, $\mathrm{E} = 111.2 \times 10^9\,\mathrm{Pa}$[64] and $\nu = 0.365$ are employed. $\nu = 0.365$ was computed using elastic constants from Carlotti et al. by $\nu = \mathrm{C}_{13}/(\mathrm{C}_{11} + \mathrm{C}_{12})$[65]. The grain size was determined by the height-height correlation length (HHCL) as determined from AFM measurements. The equalization of grain size and HHCL is justified since Owen showed the surface's lateral feature size to describe the grain size[66].

One can relate the (002) peak position to the total stress within the film. Since bulk layers were grown at the same deposition temperature, the thermal stress should be the same for all investigated films. Thus, a correction of XRD stress measurements by thermal stress is not necessary. The stress determination by means of XRD measurements

$$\sigma = \frac{E}{1-\nu}\,\frac{d_0 - d_z}{d_0} \tag{4}$$

comprises strained and unstrained vertical lattice spacing d_z and $d_0 = 5.21\,\text{Å}$[67].

The application of seed layers led to an increase of tensile stress with respect to the sample without seed layer. The tensile stress increase was computed using XRD measurements (Eq. 4) and compared to stress values obtained by the grain boundary relaxation model (Eq. 3). In particular, the ionic radius r_0 was used as a parameter to fit the GBRM stress data to the values of the XRD measurements.

Figure 9 shows the tensile stress increase as determined by the GBRM and XRD measurements. One notices a reasonable agreement between both methods of stress determination. Consequently, the tensile stress of seed layer samples resulted from smaller grains as compared to the film without seed layer.

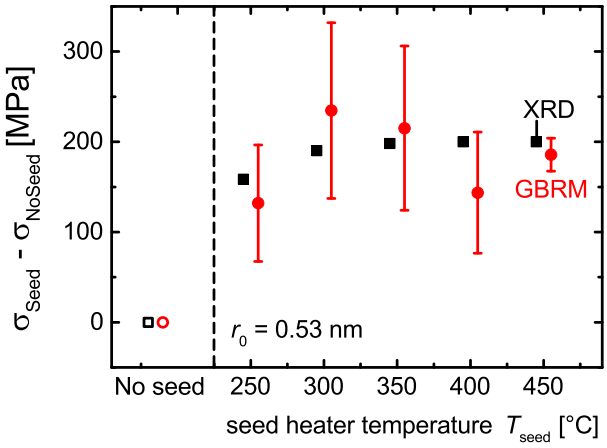

Figure 9. The relative tensile stress obtained by the grain boundary relaxation model (GBRM) (red circles) and by XRD measurements evaluating the (002) peak position (black squares) are shown for seed+bulk layers whereby seed layers were deposited at various temperatures. The value of the fit parameter r_0 is given in the graph.

C. Film structure and charge carrier mobility

The seed layer did hardly influence the electrical properties for bulk deposition temperatures of 100 °C and 200 °C (see Table I). Only for $T_{\mathrm{bulk}} = 300\,°\mathrm{C}$, a significant improvement was achieved by the application of seed layers. This difference is mainly attributed to the mobility decrease of the sample without seed layer. However, for all three bulk deposition temperatures, one observed

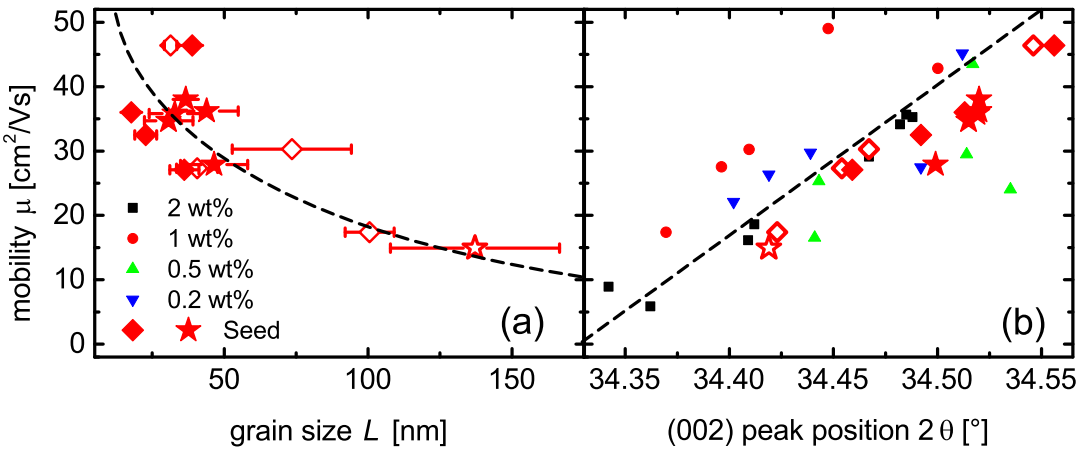

Figure 10. The charge carrier mobility is plotted as a function of grain size (a) and (002) peak position (b), respectively, for a sample without seed layer (red asterisk, open symbol) and samples with seed layer (red asterisk, closed symbols). The grain size was determined by AFM measurements. The seed layer deposition temperature was varied. Data from Berginski et al.[8] was added to figure (b). The dotted lines are guides to the eye. Note that AFM and XRD data of the bulk layer temperature variation series have not been shown in the respective Section III A.

a change of etch morphology from Type A without seed layer to Type B with seed layer (see Fig. 2). Data of Berginski et al.[8] shows that the peculiar mobility dip prevails for various TDCs and that it shifts to lower deposition temperatures when increasing the TDC. Moreover, we observed that the etch morphology was of Type A for deposition temperatures smaller or equal to the dip temperature, and that Type B prevailed for higher deposition temperatures. The change of etch morphology when using a seed layer could thus be interpreted as shifting the material from the lower to the higher temperature side of the mobility dip. This interpretation could also explain the seemingly unchanged electrical parameters for bulk deposition temperatures of 100 °C and 200 °C, because mobilities in the same range occur on either side of the mobility dip.

Figure 8 shows that the improved mobility after seed layer application was not related to seed layer thickness, i.e. thicker seed layers did not induce higher mobility values. Thus, the ameliorated electrical properties of seed+bulk layers cannot be explained by a possibly higher conductivity of seed layers that improve the whole stack of seed+bulk layer. And indeed, an exemplary measurement of a seed layer with $d_{\mathrm{seed}} = 40\,\mathrm{nm}$ and $T_{\mathrm{seed}} = 350\,^{\circ}\mathrm{C}$ revealed a mobility of $7.5\,\mathrm{cm^2\,V^{-1}\,s^{-1}}$ and a carrier concentration of $2.2 \times 10^{20}\,\mathrm{cm^{-3}}$ only.

Figure 7(d) and (e) show the FWHM of the (002) peak using Bragg-Brentano geometry and rocking curves. The Bragg-Brentano FWHM may be used to calculate the size of coherently scattering regions g by applying the Scherrer formula[68]. g is often referred to as vertical grain size[53,69]. However,the vertical grain size g is often taken as a measure for the lateral grain size although the relation between both quantities is unclear and not well-established. In this work, the peaks' FWHM in Bragg-Brentano geometry will be used without the evaluation of the Scherrer formula as a measure of crystalline quality. In addition to the films' crystalline quality, we can determine the orientation distribution of the crystallites via the rocking curve FWHM. In conclusion, lower FWHM values imply a better crystalline quality and better grain orientation.

Both FWHM values decreased with increasing T_{seed}. Thus, higher T_{seed} resulted in a better crystalline quality and grain orientation of the ZnO:Al films. The improved structural quality of the films might explain the enhanced charge carrier mobility that was observed for higher T_{seed}. However, the 250 °C seed layer sample showed only a slightly lower BB-FWHM and actually a higher RC-FWHM than the sample without seed layer although the mobility of the former was significantly higher than the mobility of the latter film. Hence, we note the particularly important result that crystallographically improved or better oriented grains are not necessarily a reason for enhanced charge carrier mobility.

It was shown before that seed layers reduced the grain size (see Fig. 7). If grain boundaries determined the mobility in the films, the mobility would be expected to decrease with decreasing grain size because the number of electron scattering grain boundaries increased. This is certainly not the case as the sample without seed layer showed the largest grain size but the lowest mobility. One interpretation of this observation might be that grain boundaries did not influence the electrical transport in the films. However, optical fits and temperature-dependent conductivity measurements suggested grain boundary scattering to be a limiting transport mechanism. These measurements furthermore suggested grain boundary scattering to be reduced as a result of seed layer application. Note also that etching characteristics supported a change in grain boundary morphology. Therefore, we propose the hypothesis that a

decrease of grain size goes along with an improvement of grain boundary morphology due to an overall ameliorated growth of the films. To support the hypothesis, Fig. 10 shows the mobility as a function of grain size (a) and (002) peak position (b), respectively. According to the GBRM, (002) peak position and grain size are correlated. Figure 10(a) and (b) should hence be redundant and give the same results. Indeed, both quantities, the grain size and the (002) peak position, show a reasonable correlation to the mobility, which supports our hypothesis that smaller grains have more but also more conductive grain boundaries. More importantly, our hypothesis leads for the presented ZnO:Al films to a counterintuitive relationship between mobility and grain size: the smaller the grains, the higher the mobility.

V. CONCLUSION

We investigated the effect of thin ($< 100\,\mathrm{nm}$), highly doped ZnO:Al seed layers that were deposited using a ZnO:Al_2O_3 target with $2\,\mathrm{wt\%}$ Al_2O_3 on subsequently grown thick ($\sim 800\,\mathrm{nm}$) and lowly doped ZnO:Al bulk layers that were sputtered from a target with $1\,\mathrm{wt\%}$ Al_2O_3. The application of seed layers for the subsequent growth of bulk films allowed for a reduction of heater temperature by approximately $100\,^\circ\mathrm{C}$ without deteriorating electrical, optical, and etching properties. We suspect the dopant aluminum to act as a surfactant that increases the surface diffusion length. The higher aluminum content in the seed layers led via the surfactant effect to preferential 2D-growth. The 2D-growth is characterized by a reduction of grain size and surface roughness. This beneficial growth mode is adopted by the subsequently grown bulk layers with lower aluminum content. The application of seed layers induced higher tensile stress. The tensile stress was interpreted in terms of the grain boundary relaxation model. In the framework of this model, the augmented tensile stress applying seed layers resulted from reduced grain size. Furthermore, temperature-dependent conductivity measurements, optical fits, and etching characteristics suggested that the use of seed layers reduced grain boundary scattering. Thus, the application of seed layers significantly improved the grain boundary morphology resulting in higher mobilities and more suitable etching characteristics. Particularly noteworthy is the counterintuitive fact that smaller grains led to a higher charge carrier mobility. A seed layer thickness of $5\,\mathrm{nm}$ was sufficient to induce the beneficial effects with regard to electrical, optical, and etching properties.

ACKNOWLEDGMENTS

We would like to thank O. Tremmel, W. Appenzeller, U. Gerhards, H. Siekmann, D. Weigand, A. Bauer, and M. Ziegner for technical assistance and our partners in the joint project LIST for fruitful discussions. Financial support by the German Ministry BMWi (contract no. 0325299) is gratefully acknowledged.

REFERENCES

[1] C. G. Granqvist, Solar Energy Materials and Solar Cells **91**, 1529 (2007).
[2] C. G. Granqvist, *Handbook of inorganic electrochromic materials* (Elsevier, 1995).
[3] D. S. Ginley and C. Bright, MRS Bulletin **25**, 15 (2000).
[4] K. L. Chopra, P. D. Paulson, and V. Dutta, Progress in Photovoltaics: Research and Applications **12**, 69 (2004).
[5] K. Ellmer, A. Klein, and B. Rech, *Transparent conductive zinc oxide: basics and applications in thin film solar cells*, Vol. 104 (Springer, 2007).
[6] A. G. Aberle, Thin Solid Films **517**, 4706 (2009).
[7] J. ichi Nomoto, T. Hirano, T. Miyata, and T. Minami, Thin Solid Films **520**, 1400 (2011).
[8] M. Berginski, J. Hüpkes, M. Schulte, G. Schöpe, H. Stiebig, B. Rech, and M. Wuttig, Journal of Applied Physics **101**, 074903 (2007).
[9] R. Klenk, J. Klaer, C. Köble, R. Mainz, S. Merdes, H. Rodriguez-Alvarez, R. Scheer, and H. Schock, Solar Energy Materials and Solar Cells **95**, 1441 (2011).
[10] P. Reinhard, A. Chirila, P. Blosch, F. Pianezzi, S. Nishiwaki, S. Buechelers, and A. Tiwari, IEEE Journal of Photovoltaics **3**, 572 (2013).
[11] H. Sai, H. Jia, and M. Kondo, Journal of Applied Physics **108**, 044505 (2010).
[12] M. Boccard, C. Battaglia, S. Hänni, K. Söderström, J. Escarré, S. Nicolay, F. Meillaud, M. Despeisse, and C. Ballif, Nano Letters (2012), 10.1021/nl203909u, http://pubs.acs.org/doi/pdf/10.1021/nl203909u.
[13] S. Faÿ, J. Steinhauser, S. Nicolay, and C. Ballif, Thin Solid Films **518**, 2961 (2010).
[14] J. I. Owen, J. Hüpkes, H. Zhu, E. Bunte, and S. E. Pust, physica status solidi (a) **208**, 109 (2011).
[15] S. E. Pust, J.-P. Becker, J. Worbs, S. O. Klemm, K. J. J. Mayrhofer, and J. Hüpkes, Journal of The Electrochemical Society **158**, D413 (2011), http://jes.ecsdl.org/content/158/7/D413.full.pdf+html.
[16] O. Kluth, G. Schöpe, J. Hüpkes, C. Agashe, J. Müller, and B. Rech, Thin Solid Films **442**, 80 (2003).
[17] W. Böttler, V. Smirnov, J. Hüpkes, and F. Finger, physica status solidi (a) **209**, 1144 (2012).
[18] D. Köhl, M. Luysberg, and M. Wuttig, Journal of Physics D: Applied Physics **43**, 205301 (2010).
[19] D. Köhl, G. Natarajan, and M. Wuttig, Journal of Physics D: Applied Physics **45**, 245302 (2012).
[20] W. Dewald, V. Sittinger, B. Szyszka, F. Säuberlich, B. Stannowski, D. Köhl, P. Ries, and M. Wuttig, Thin Solid Films **534**, 474 (2013).
[21] F. Claeyssens, C. L. Freeman, N. L. Allan, Y. Sun, M. N. R. Ashfold, and J. H. Harding, J. Mater. Chem. **15**, 139 (2005).
[22] F. D'Heurle and J. Harper, Thin Solid Films **171**, 81 (1989).
[23] H. Windischmann, Critical Reviews in Solid State and Materials Sciences **17**, 547 (1992), http://dx.doi.org/10.1080/10408439208244586.
[24] Note that this work and its results are also published in the PhD thesis of the corresponding author.
[25] T. Bronger, *Electronic properties of μc-Si:H layers investigated with Hall measurements*, Ph.D. thesis, RWTH Aachen University (2007).
[26] J. Woerdenweber, T. Merdzhanova, T. Zimmermann, A. Flikweert, H. Stiebig, W. Beyer, and A. Gordijn, Journal of Non-Crystalline Solids **358**, 2183 (2012).

[27] A. J. Flikweert, T. Zimmermann, T. Merdzhanova, D. Weigand, W. Appenzeller, and A. Gordijn, Journal of Physics D: Applied Physics **45**, 015101 (2012).
[28] M. Theiss, *Hard and Software for Optical Spectroscopy*, Dr. Berhard-Klein-Straße 110, 52078 Aachen, Germany, www.mtheiss.com.
[29] D. Mergel and Z. Qiao, Journal of Physics D: Applied Physics **35**, 794 (2002).
[30] Z. Qiao, C. Agashe, and D. Mergel, Thin Solid Films **496**, 520 (2006).
[31] Z.-C. Jin, I. Hamberg, and C. G. Granqvist, Journal of Applied Physics **64**, 5117 (1988).
[32] J. Steinhauser, S. Fay, N. Oliveira, E. Vallat-Sauvain, and C. Ballif, Applied Physics Letters **90**, 142107 (2007).
[33] J. Steinhauser, S. Faÿ, N. Oliveira, E. Vallat-Sauvain, D. Zimin, U. Kroll, and C. Ballif, physica status solidi (a) **205**, 1983 (2008).
[34] A. Bikowski and K. Ellmer, Journal of Applied Physics **114**, 063709 (2013), http://dx.doi.org/10.1063/1.4817376.
[35] S. Brehme, F. Fenske, W. Fuhs, E. Nebauer, M. Poschenrieder, B. Selle, and I. Sieber, Thin Solid Films **342**, 167 (1999).
[36] H. Fujiwara and M. Kondo, Phys. Rev. B **71**, 075109 (2005).
[37] N. Ehrmann and R. Reineke-Koch, Thin Solid Films **519**, 1475 (2010).
[38] R. J. Mendelsberg, G. Garcia, and D. J. Milliron, Journal of Applied Physics **111**, 063515 (2012), http://dx.doi.org/10.1063/1.3695996.
[39] A. Pflug, V. Sittinger, F. Ruske, B. Szyszka, and G. Dittmar, Thin Solid Films **455–456**, 201 (2004).
[40] F. Ruske, A. Pflug, V. Sittinger, B. Szyszka, D. Greiner, and B. Rech, Thin Solid Films **518**, 1289 (2009).
[41] D. Greiner, N. Papathanasiou, A. Pflug, F. Ruske, and R. Klenk, Thin Solid Films **517**, 2291 (2009).
[42] N. Sommer, S. Götzendörfer, F. Köhler, M. Ziegner, and J. Hüpkes, Thin Solid Films **568**, 25 (2014).
[43] S. Schönau, F. Ruske, S. Neubert, and B. Rech, Applied Physics Letters **103** (2013), http://dx.doi.org/10.1063/1.4829999.
[44] H. Brooks, *Advances in electronics and electron physics* (Academic Press Inc., 1955).
[45] R. Dingle, Philosophical Magazine Series 7 **46**, 831 (1955), http://www.tandfonline.com/doi/pdf/10.1080/14786440808561235.
[46] T. Pisarkiewicz, K. Zakrzewska, and E. Leja, Thin Solid Films **174**, 217 (1989).
[47] J. Ziman, *Electrons and Phonons: The Theory of Transport Phenomena in Solids*, Oxford Classic Texts In The Physical Sciences (Oxford University Press, 2001).
[48] P. B. Allen, in *Quantum Theory of Real Metals*, edited by J. R. C. S. G. Louie (Kluwer Academic Publishers, 1996) Chap. 17, pp. 219–250.
[49] S. Hunklinger, *Festkörperphysik* (Oldenbourg, 2007).
[50] R. Stratton, Journal of Physics and Chemistry of Solids **23**, 1177 (1962).
[51] R. Stratton, Phys. Rev. **125**, 67 (1962).
[52] N. Sommer, J. Hüpkes, and U. Rau, (2015), to be published.
[53] R. Cebulla, R. Wendt, and K. Ellmer, Journal of Applied Physics **83**, 1087 (1998).
[54] J. Hinze and K. Ellmer, Journal of Applied Physics **88**, 2443 (2000).
[55] M. Suchea, S. Christoulakis, N. Katsarakis, T. Kitsopoulos, and G. Kiriakidis, Thin Solid Films **515**, 6562 (2007).
[56] L. Ding, M. Boccard, G. Bugnon, M. Benkhaira, S. Nicolay, M. Despeisse, F. Meillaud, and C. Ballif, Solar Energy Materials and Solar Cells **98**, 331 (2012).
[57] M. Copel, M. C. Reuter, E. Kaxiras, and R. M. Tromp, Phys. Rev. Lett. **63**, 632 (1989).
[58] J. Massies and N. Grandjean, Phys. Rev. B **48**, 8502 (1993).
[59] D. Kandel and E. Kaxiras, Phys. Rev. Lett. **75**, 2742 (1995).
[60] J. A. Thornton, Journal of Vacuum Science & Technology **11**, 666 (1974).
[61] M. Warzecha, *Zinkoxid: Einfluss von Dotierung und Legierungen auf elektro-optische Eigenschaften, auf das Ätzverhalten und auf die Tempernachbehandlung*, Ph.D. thesis, RWTH Aachen University (2014).
[62] K.-N. Tu and R. Rosenberg, *Analytical Techniques for Thin Films: Treatise on Materials Science and Technology*, Vol. 27 (Elsevier, 2013).
[63] J. D. Finegan and R. W. Hoffman, Journal of Applied Physics **30**, 597 (1959).
[64] S. O. Kucheyev, J. E. Bradby, J. S. Williams, C. Jagadish, and M. V. Swain, Applied Physics Letters **80**, 956 (2002).
[65] G. Carlotti, D. Fioretto, G. Socino, and E. Verona, Journal of Physics: Condensed Matter **7**, 9147 (1995).
[66] J. I. Owen, *Growth, Etching, and Stability of Sputtered ZnO:Al for Thin-Film Silicon Solar Cells*, Ph.D. thesis, RWTH Aachen (2011).
[67] U. Özgür, Y. I. Alivov, C. Liu, A. Teke, M. A. Reshchikov, S. Doğan, V. Avrutin, S.-J. Cho, and H. Morkoç, Journal of Applied Physics **98**, 041301 (2005), http://dx.doi.org/10.1063/1.1992666.
[68] P. Scherrer, Nachrichten von der Gesellschaft der Wissenschaften zu Göttingen, Mathematisch-Physikalische Klasse **1918**, 98 (1918).
[69] M. Berginski, *Lichtstreuende Oberflächen, Schichten und Schichtsysteme zur Verbesserung der Lichteinkopplung in Silizium-Dünnschichtsolarzellen*, Ph.D. thesis, RWTH Aachen University (2008).